

# Behavior of Cold-Formed High Strength Steel Rectangular and Square Hollow Sections under Combined Compression and Bending

Jia-Lin Ma<sup>1</sup>, Tak-Ming Chan, M.ASCE<sup>2\*</sup> Ben Young, F.ASCE<sup>3</sup>

## Abstract:

High strength steel is gaining more attention from engineers due to its high strength-to-weight ratio and cost effectiveness. However, the research on cold-formed high strength steel (CFHSS) tubular members subjected to combined compression and bending is limited. This paper, therefore, presents an experimental investigation on this combined loading scenario. The test specimens consisted of 5 square hollow section sizes and 2 rectangular hollow section sizes. The nominal proof stresses of the test specimens were between 700 MPa to 900 MPa. A total of 51 short beam-columns were tested to investigate the behavior of CFHSS rectangular and square hollow sections subjected to combined compression and bending. A set of different initial loading eccentricities were adopted to attain a wide range of bending-to-compression ratios. The compression and bending capacities, load-deformation histories and failure modes of the test specimens were reported. Based on the test results, the design methods described in American, Australian and European codes were evaluated. The finite-element modelling methodology for CFHSS tubular beam-columns was also presented.

**Keywords:** Cold-formed steel; Finite element; High strength steel; Beam-column; Combined compression and bending test; Tubular section; Hollow section.

<sup>1</sup> Postdoctoral Research Fellow, Dept. of Civil and Environmental Engineering, Tongji Univ., Shanghai 200082, China; Building Research Center, Vanke Co. Ltd., Huanmei Rd., Shenzhen, China. E-mail: kmconi@hotmail.com

<sup>2</sup> Assistant Professor, Dept. of Civil and Environmental Engineering, The Hong Kong Polytechnic University, Hong Kong, China (corresponding author). E-mail: tak-ming.chan@polyu.edu.hk

<sup>3</sup> Professor, Dept. of Civil and Environmental Engineering, The Hong Kong Polytechnic University, Hong Kong, China. E-mail: [ben.young@polyu.edu.hk](mailto:ben.young@polyu.edu.hk) (Formerly, Dept. of Civil Engineering, The Univ. of Hong Kong, Pokfulam Rd, Hong Kong. E-mail: young@hku.hk)

## Introduction

Cold-formed high strength steel (CFHSS) tubular sections have great potential in structural

30 engineering due to their high strength-to-weight ratios, easy fabrication, low material costs and strong  
31 resistance against torsional buckling. High strength steel (HSS) tubes with nominal yield strengths of  
32 700 MPa and 900 MPa as well as other steel grades are now commercially available. Investigations on  
33 fabricated HSS members were started several decades ago and the corresponding member structural  
34 behavior and design guidelines have been evaluated by researchers worldwide (Beg and Hladnik 1996;  
35 Lee et al. 2012; Nishino and Tall 1970; Rasmussen and Hancock 1995; Usami and Fukumoto 1982;  
36 Yu and Tall 1968). To obtain effective structural design for HSS tubular members with nominal yield  
37 strength ranging from 460 MPa to 1100 MPa, extensive research studies have been carried out to  
38 determine the material properties and residual stresses of HSS tubular members (Ma et al. 2015, Hu  
39 and Chung 2017) and to examine the behavior of these members under various types of loading (Ma  
40 et al. 2016a, b, Wang and Gardner 2017 and Fang and Chan 2018). Based on the existing research data,  
41 design recommendations for cross-section classifications (Chan et al. 2015) and predictions of the  
42 ultimate loads of HSS tubular members subject to axial compression (Ma et al. 2018a), bending (Ma  
43 et al. 2017b, Wang et al. 2017) and combined compression and bending (Gkantou et al. 2017) have  
44 been proposed. The above research studies primarily cover the HSS tubular members with square,  
45 rectangular and circular shaped cross-sections. The authors initiated a research program on CFHSS, in  
46 which the material properties, the cross-sectional residual stress distributions, geometric local  
47 imperfections, resistances against compression and resistances against bending were studied (Ma et al.  
48 2015; Ma et al. 2016a; Ma et al. 2016b; Ma et al. 2017a; Ma et al. 2018). The structural behavior  
49 against combined compression and bending of CFHSS beam-columns are rarely found in literatures  
50 thus this paper describes the experimental investigations conducted for RHS and SHS made of CFHSS  
51 under combined compression and bending. The current codes of practice are evaluated based on the  
52 experimental results and design recommendations are proposed in this paper. The finite-element (FE)  
53 modelling methodology is also discussed in this research.

## 55 **Experimental Investigation**

### 56 ***Test Specimens***

57 The beam-column specimens in this paper comprises of two different grades: namely, H-series and V-  
58 series. The nominal proof stresses of the two series are 700 and 900 MPa for H and V-series,  
59 respectively. Five square hollow section sizes and two rectangular hollow section sizes are investigated  
60 in this study. The SHS and RHS are labelled as “Series,  $B$ ,  $H$ ,  $t$ ”, in which  $B$ ,  $H$  and  $t$  are the width,  
61 depth and thickness of the sections, respectively. The combined compression and bending tests for  
62 RHS were conducted for both major axis and minor axis.

63  
64 The material strength of CFHSS is related to both the base material strength and cold-working  
65 enhancements. Usually there is no yield plateau for the stress-strain curves of CFHSS material due to  
66 the work hardening effect. The 0.2% proof stress  $\sigma_{0.2}$  is therefore taken as the yield stress. The tensile  
67 coupons from both flat and corner portions of the sections were tested since corner strength  
68 enhancements are significant for cold-formed sections. The material testing methodology and the  
69 obtained material properties for this batch of CFHSS have been described in Ma et al. (2015). The  
70 corresponding 0.2% modulus of elasticity  $E$ , 0.2% proof stresses  $\sigma_{0.2}$  and ultimate stresses  $\sigma_u$  are  
71 reported in Table 1. As shown in the last column of the table, the material strengths for corner regions  
72 are generally higher than the ones for flat portions.

73  
74 All the beam-column specimens were cold-sawed from 3 meter long tubes. The specimens were milled  
75 flat on both ends and welded to 25 mm thick end plates. For each cross-section, five to seven short  
76 beam-columns were prepared to be loaded under different initial loading eccentricities, in which  
77 different combinations of axial compression-to-bending moment ratios were achieved. The specimens  
78 were labelled as “Series,  $B$ ,  $H$ ,  $t$ , BC,  $e$ ” and  $e$  is the nominal initial loading eccentricity adopted. The  
79 nominal cross-section geometry loading eccentricities could thus be identified (e.g. H120×200×5-BC-  
80 e15 stands for a beam-column ‘BC’ specimen, which bends in its major axis and is loaded with a

nominal eccentricity of 15 mm at both ends.) The typical measured length and dimension of specimens are shown in Table 2.  $R$  and  $r$  are the outer and inner corner radii for the SHS and RHS.

### **Instrumentation**

The combined bending and compression loading effects were achieved through applying compression forces with certain eccentricities on both ends of the beam-column specimens. The applied eccentricities lead to uniform bending moment and single-curvature along the member length. The test rig and setup are shown in Fig. 1. A hydraulic testing machine with 5000kN capacity was used to apply compression forces to the specimens. Two parallel knife edges were used at both ends of the specimens and the effective length equals to the pin-to-pin length of the two knife edges. The boundary condition was provided by sets of pit plates and wedge plates. The ends of the specimens were free to rotate in the bending plane. Slot holes were machined on the wedge plates to allow the adjustment of loading eccentricities. Similar setup has been adopted by various researchers for different materials and section shapes (Gardner et al. 2011; Huang and Young 2014; Sheehan et al. 2012; Zhao et al. 2016; Zhu and Young 2006). In this study, the upper pit plate was fixed to the top of the self-reaction frame and the lower pit was locked to the machine jack using a lockable sitting.

As shown in Fig. 1, three displacement transducers (two at the front and one at the back of the specimen) were installed vertically to measure both the axial shortening and end-rotation of the specimens. Two transducers were applied at mid-height of the specimens to measure the horizontal deflections. Additionally, four strain gauges were attached on the two faces in the bending plane to determine the initial loading eccentricities, as shown in Fig. 2. Displacement-control was adopted in testing and a fixed loading rate of 0.3 mm/min was used for all the specimens. The readings from machine, transducers and strain gauges were recorded by a data acquisition system at a regular interval. Through pausing the tests near ultimate level for 90 seconds, the static responses of the beam-columns were obtained.

## **Determination of loading eccentricities**

To measure the loading eccentricities, the specimens were setup on the wedge plates with designated eccentricities and preloaded with 3 to 5 kN to ensure the full contact between bolted specimens and pit plates. The beam-columns were set to the up-straight positions based on the alignments from a total station.

The test specimens were carefully prepared with the centers accurately marked at the mid-height on the front faces. The adopted eccentricity was first measured by the total station through comparing the space coordinates of the center point on the front face of the specimen and the front center of the knife edges. For loading eccentricities smaller than 50 mm, the adopted eccentricity values were carefully examined with the measurements from the strain gauge readings. The small loading eccentricity values  $(e + \delta_0)$  can be calculated more accurately from  $(e + \delta_0) = EI\kappa / P - \delta_y$ , in which  $\delta_0$  is the initial global geometric imperfection,  $EI$  is the bending stiffness of the section,  $\kappa$  is the curvature calculated from the strain gauge readings,  $P$  is the applied axial force and  $\delta_y$  is the horizontal deflection calculated from the absolute average readings of the two horizontal transducers. As the specimens are short, thus the global geometric imperfections  $\delta_0$  are negligible. The measured eccentricity values  $e$  are summarized in Table 3.

## **Test results**

A total of 51 beam-column specimens were tested in this study and they were grouped into 9 series according to the section sizes. In each series, one specimen was loaded concentrically whereas the other beam-columns were loaded with different eccentricities. Table 3 summarizes the nominal and measured eccentricities, ultimate axial compression loads  $P_u$ , ultimate moments at specimen ends  $M_{\text{end,u}} = P_u e$  and ultimate moments at mid-height of specimens  $M_{\text{mid,u}} = P_u (e + \delta_y)$ . Repeated tests

were conducted and they were labelled with a '#' after the nominal eccentricity. The axial load  $P$  versus end rotation  $\theta$  histories were recorded and typical curves are shown in Fig. 3 and Fig. 4 for H120×120×4-BC and V80×80×4-BC, respectively. The measured initial loading eccentricities are also given along with the  $P$ - $\theta$  curves.

Generally in prevalent design codes, the allowed grade of HSS is limited to 690 and 700 MPa (ANSI/AISC 360-10 2010; AS 4100-A1 2012; EN 1993-1-12 2007), and the current design methods for beam-columns are still based on the previous researches from normal grade steel. Thus it is worthwhile to evaluate the codes for HSS beam-columns with grades higher than 700 MPa. To make a full comparison to the  $P$ - $M$  interaction curves, the moment capacity of the sections are needed. In previous study (Ma et al. 2016b), the authors investigated the bending behaviour for this batch of CFHSS sections using four-point-bending tests. The obtained moment capacity results for this batch of sections are shown in Table 4, in which 'B' denotes a four-point-bending test specimen.

The obtained test results are plotted against the codified beam-column design interaction curves in Fig. 5. In the figures, the experimental ultimate loads  $P_u$  are normalized to the average squash load  $P_y = Af_y$  and the end moments  $M_{end,u}$  are normalized to the average plastic moment  $M_p = W_p f_y$  of the sections. The data points from tests are plotted against the design interaction curves from ANSI/AISC 360-10 (2010), EN 1993-1-1 (2005) and AS 4100 (1998). The test-to-prediction ratios of specimens are evaluated through comparing the test data points to the data points on the interactions curves which have the same initial loading eccentricities  $e$ , as shown in Fig. 6. The mean  $P_u/P_{pred}$  values and the corresponding coefficient of variance (COV) values are given in Table 5.

ANSI/AISC 360-10 (2010) uses a two-phase relationship to describe the interaction of axial loads and bending moments, as shown in Eq. (1). The design axial load  $P_u$  and bending moment  $M_u$  are proportioned to the nominal capacity under pure compression  $P_n$  and predicted nominal capacity under

158 pure bending  $M_n$ , respectively. For the case of single uniform curvature and uniaxial bending, the  
 159 second-order effect can be considered through applying the amplification factor  $1/(1-P/P_{cr})$  to the end  
 160 moment  $M_{end,u}$ . The second-order design moment  $M_u$  for the beam-column specimens is thus derived.  
 161 As the beam-column specimens in this paper are relatively short thus the average amplification factor  
 162 for second-order effect is close to unity (1.039). The mean value for  $P_u/P_{AISC}$  is 1.13 and the  
 163 corresponding COV value is 0.081.

$$164 \quad \begin{cases} \frac{P_u}{P_n} + \frac{8}{9} \frac{M_u}{M_n} \leq 1 & \text{for } \frac{P_u}{P_n} \geq 0.2 \\ \frac{P_u}{2P_n} + \frac{M_u}{M_n} \leq 1 & \text{for } \frac{P_u}{P_n} < 0.2 \end{cases} \quad (1)$$

165 The design equation in AS 4100 (1998) is shown in Eq. (2) and can be transformed to Eq.(3). The  
 166 denominators in Eq.(3) are the corresponding member capacity under pure compression and pure  
 167 bending. The amplification factor for bending moment is the same to the one in ANSI/AISC 360-10  
 168 (2010). The second-order effect is not significant for this batch of CFHSS short beam-columns. The  
 169 mean value for  $P_u/P_{AS4100}$  is 1.21 and the corresponding COV value is 0.075.

$$170 \quad M_u \leq M_n \left( 1 - \frac{P_u}{P_n} \right) \quad (2)$$

$$171 \quad \frac{P_u}{P_n} + \frac{M_u}{M_n} \leq 1 \quad (3)$$

172 EN 1993-1-1 (2005) adopts similar design methods whereas an interaction factor  $k_{yy}$  is used, as shown  
 173 in Eq. (4). Different from ANSI/AISC 360-10 (2010) and AS 4100 (1998), the design moment in the  
 174 equation of EN 1993-1-1 (2005) is based on first-order moments (Ziemian 2010), thus  $M_{end,u}$  is used  
 175 as the design required moment. To calculate the interaction factor, two methods are provided and  
 176 Method 1 in Annex A is adopted in this study. The mean value for  $P_u/P_{EC3}$  is 1.16 and the corresponding  
 177 COV value is 0.067.

$$178 \quad \frac{P_u}{P_n} + k_{yy} \frac{M_{end,u}}{M_n} \leq 1 \quad (4)$$

To summarize, ANSI/AISC 360-10 (2010) provides the closest prediction for this batch of CFHSS beam-columns. In Fig. 5, it is observed that the end-points of interactions curves (pure compression, pure bending) are generally conservative, especially for the moment capacities of sections against pure bending. Section compactness were considered in calculation of the end points as well as the capacities of beam-columns using different eccentricities. Slender sections generally yield smaller pure bending and pure compression capacities when compared to squash loads and plastic moments. According to the specifications, the predictions for end points of interaction curves are more conservative for sections with small slenderness, such as H50×100×4, H80×80×4 and V80×80×4. The pure compression capacities of those sections usually exceed the squash load  $P_y$  due to corner strength enhancements. As explained in Ma et al. (2016a) and Ma et al. (2016b), generally the specifications give conservative predictions to beams and columns with compact sections while the predictions are slightly unconservative for columns with slender sections. Thus for short beam-columns, the predictions become more reliable when accurate end points on interactions curves are used. Hence, improvements are possible if modifications are made to the end-points of interactions curves and provide more accurate predictions for CFHSS columns and beams. Based on the test results, a reliability analysis was conducted and results shown that the codes are reliable since the obtained reliability index are all greater than the target value of 2.5 (Table 5).

### ***Finite Element Modeling***

Based on the experimental work on the CFHSS tubular beam-columns, it is imperative to conduct numerical campaign to generate further numerical tests results with an aim to comprehensively reviewing the current design methods. This section therefore, details the finite element modelling methodology including the choice of material properties, geometric imperfections, residual stresses and boundary conditions which could be adopted in similar investigations on cold-formed sections and to inform further parametric investigation.

205 In the FE modeling, the true stress versus log plastic strain relationship obtained from CFHSS  
206 constitutive model (Ma et al. 2015) was adopted. The S4R shell element with 4 nodes and reduced  
207 integration was used (ABAQUS 2013). The mesh seed size was set to  $(B+H)/30$  for all the SHS and  
208 RHS. The measured maximum local imperfection values were used as reported in Ma et al. (2016a).  
209 Through elastic buckling analysis, the lowest elastic eigenmode shape was chosen as the local  
210 geometric imperfection profile which was then scaled to the measured local imperfection values.  
211 Similar modelling methodology has been successfully used for CFHSS stub columns and beams (Ma  
212 et al. 2016a; Ma et al. 2016b; Chan and Ben 2019). The specimens were short so that the influence  
213 from global imperfection should be insignificant. As the tensile coupon specimens were clamped  
214 before tests, the large bending residual stress has been approximated and included in the tested  
215 constitutive relationships (Rasmussen and Hancock 1993). The largest measured longitudinal  
216 membrane residual stresses of HSS tubes were reported to be only about 20% of the 0.2% proof stresses.  
217 Thus it is not necessary to include the geometric global imperfections and the residual stresses in the  
218 model. Similar conclusions were verified in previous studies (Ma et al. 2016a; Ma et al. 2016b).

219

220 The measured corner material stress-strain curves were also used to describe the corner region material  
221 properties as the cold-working effect of SHS and RHS makes the corner materials stronger but less  
222 ductile than their flat counterparts. Rossi et al. (2013) investigated the corner material properties for  
223 carbon steel and stainless steel, and proposed a new material model to predict the strength  
224 enhancements in cold-formed sections. Improving FE model predictions through extending corner  
225 properties as  $2t$  in the FE model has been verified in the authors' previous investigations on columns  
226 and beams (Ma et al. 2016a. Ma et al. 2016b). Similar observations were given in Gardner and  
227 Nethercot 2004. Therefore, this methodology is also adopted in the study (Fig. 7).

228

229 A set of knife-edge boundary condition was used in the tests. At the end of the specimens, the endplate,  
230 wedge plate and the pin system have a total height of 87.5 mm. Thus during modelling, two reference

points were coupled to the nodes of top and bottom cross-section ends and then offset by 87.5 mm longitudinally away from the ends. Afterwards in the bending plane, the reference points were offset horizontally by measured initial eccentricity  $e$  to reach the loading point. The exact position of the reference point is illustrated in Fig. 8. On the two reference points of each beam-column model, the rotation in the bending plane was allowed and the top reference point was also free to move along the longitudinal direction of specimen. The boundary conditions and the effective lengths were then successfully modelled. Compression forces were applied through the top reference point and the geometric non-linearity was enabled throughout the FE analysis. A smooth load-deformation history was obtained for the FE model by limiting the maximum step increment in the analysis.

From comparison, the test-to-FE ultimate capacity ratios are tabulated in the last column of Table 5. The mean  $P_u/P_{FE}$  value is 0.98 and the corresponding COV value is 0.042, showing that the ultimate capacities of beam-column specimens are successfully replicated by the FE models. Fig. 9 shows the comparison of load-end rotation curves for H50×100×4-BC. Fig. 10 and Fig. 11 show the comparison of failure modes between tests and FE. The FE results thus showed that the model is accurate in replicating the structural behavior of CFHSS tubular beam-columns.

To summarize, the FE model for CFHSS tubular beam-columns adopted the material model and local imperfection measurement from Ma et al. (2015), Ma et al. (2016a). The influence from global imperfection and residual stresses were neglected whereas the cold-working effect of SHS and RHS was considered by inputting the measured corner material model to the defined corner regions. The model is capable of replicating the ultimate capacities, load-end rotation curves and failure modes and thus is suggested to be used in future parametric study for CFHSS tubular beam-columns.

## **Conclusions**

A total of 51 cold-formed high strength steel short beam-column tests were conducted for 5 square

hollow section sizes and 2 rectangular hollow section sizes. For RHS, both the major axis and minor axis combined loading conditions were examined. The test setup and experimental procedures of short beam-column tests have been described. The test results were compared to the predictions from codified design methods and the comparison revealed that the codes are generally conservative by 13% to 21% on average. Closest prediction was given by AISC 303-10 (2005), in which a two-phase  $P$ - $M$  interaction curve is used, thus is suggested to be used for CFHSS short beam-columns. The conservative predictions for compact CFHSS sections under pure compression and bending leads to conservative predictions on loading capacities for the short beam-columns. Improvements on the accuracy of current design methods for beam-columns are possible if the prediction of interaction curve end-points (the predicted capacity for pure compression and pure bending of the beam-columns) can be improved. More data will be needed to calibrate the end points on interactions curves as well as the corresponding interaction factors.

The methodology on the FE modelling of the CFHSS tubular beam-columns has been explained. The accuracy of the model has been justified from the comparison of load-end rotation curves, ultimate capacities and failure modes. Based on the verified finite element model, parametric study could be conducted to generate further numerical test data in the future. A larger sample pool can be generated to cover a wider range of cross-section slenderness and different steel grades, which can be helpful to propose improved and efficient design rules for CFHSS tubular beam-columns.

## Acknowledgements

The authors would like to thank the technicians and the final year undergraduate student Mr. Ho-Chun Chui from the Department of Civil Engineering at The University of Hong Kong for their assistance in helping the experimental works. The authors are also grateful to Rautaruukki for supplying the cold-formed high strength tubular test specimens. The research work described in the article was supported by a grant from the Research Grants Council of the Hong Kong Special Administrative Region, China

283 (Project no. 17212115). The authors are also grateful for the support from the Chinese National  
284 Engineering Research Centre for Steel Construction (Hong Kong Branch) at The Hong Kong  
285 Polytechnic University.

286

287 **Table 1.** SHS, RHS tensile coupon test results (Ma et al. (2015))

288 **Table 2.** Typical dimensions for specimens

289 **Table 3.** Beam-column test results

290 **Table 4.** Measured bending moment capacities (Ma et al. (2016b))

291 **Table 5.** Comparison with codes and FE results

292

293

294 **Fig. 1 .** Experimental and schematic arrangement for beam-column tests

295 **Fig. 2 .** Arrangement of strain gauges for beam-columns

296 **Fig. 3 .** Axial load versus end rotation curves for H120×120×4-BC

297 **Fig. 4 .** Axial load versus end rotation curves for V80×80×4-BC

298 **Fig. 5 .** Comparison of interaction curves

299 **Fig. 6 .** Illustration for comparison between tests and predictions from codes

300 **Fig. 7 .** Extension of corner material property to flat portions

301 **Fig. 8 .** Location of reference point

302 **Fig. 9 .** Experimental and numerical load-deflection curves for H50×100×4-BC

303 **Fig. 10 .** Comparison of failure modes between test and numerical results for H120×120×4-BC-e30

304 **Fig. 11 .** Comparison of failure modes between test and numerical results for H120×200×5-BC-e60

305

306

## 307 **Notation**

308 *The following symbols are used in this paper:*

309  $A$  = Gross cross section area;  
 310  $B$  = Overall width of cross section;  
 311  $E$  = Young's modulus of steel;  
 312  $e$  = Loading eccentricity;  
 313  $f_y$  = Yield stress of steel;  
 314  $H$  = Overall depth of cross section;  
 315  $I$  = Second moment of area;  
 316  $k_{yy}$  = Interaction factor from EN 1993;  
 317  $L$  = Length of beam column;  
 318  $M$  = Bending moment;  
 319  $M_{\text{end,u}}$  = Experimental ultimate moment at specimen ends;  
 320  $M_{\text{mid,u}}$  = Experimental ultimate moment at mid-height;  
 321  $M_p$  = Plastic moment of cross-section;  
 322  $M_u$  = Experimental ultimate moment;  
 323  $P$  = Axial load;  
 324  $P_{\text{AISC}}$  = Nominal strength (unfactored design strength) from ANSI/AISC 360-10;  
 325  $P_{\text{cr}}$  = Elastic critical buckling strength of the member;  
 326  $P_{\text{AS4100}}$  = Nominal strength (unfactored design strength) from AS 4100;  
 327  $P_{\text{EC3}}$  = Nominal strength (unfactored design strength) from EN 1993;  
 328  $P_{\text{FE}}$  = Finite element ultimate load;  
 329  $P_n$  = Nominal design axial load;  
 330  $P_{\text{pred}}$  = Predicted ultimate load from codified design methods;  
 331  $P_y$  = Squash load of cross-section;  
 332  $P_u$  = Experimental ultimate load;  
 333  $R$  = Outer corner radius of square and rectangular hollow sections;  
 334  $r$  = Inner corner radius of square and rectangular hollow sections;  
 335  $t$  = Plate thickness;  
 336  $W_{\text{pl}}$  = Plastic section modulus;  
 337  $\delta_0$  = Measured global geometric imperfection;  
 338  $\delta_y$  = Horizontal deflection at mid-height of specimen;  
 339  $\kappa$  = Curvature of specimen;  
 340  $\sigma_u$  = Ultimate tensile strength;  
 341  $\sigma_{0.2}$  = 0.2% tensile proof stress;  
 342  $\sigma_{0.2f}$  = 0.2% tensile proof stress from flat tensile coupon;

343  $\sigma_{0.2c}$  = 0.2% tensile proof stress from corner tensile coupon;  
 344  $\theta$  = End rotation of specimen;  
 345

## 346 References

- 347 ABAQUS [Computer software]. Dassault Systèmes, Providence, RI.  
 348 AISC (American Institute of Steel Construction). (2005). "Code of Standard Practice for Steel Buildings and Bridges." AISC 303-10, Chicago  
 349  
 350 ANSI/AISC (American National Standards Institute/American Institute of Steel Construction). (2010). "Specification for structural steel buildings." ANSI/AISC 360-10, Chicago.  
 351  
 352 AS (Australian Standard). (1998). "Steel structures." AS 4100, Sydney, Australia.  
 353 AS (Australian Standard). (2012). "Amendment No. 1 to AS 4100-1998 steel structures." AS 4100-A1, Sydney, Australia.  
 354 Beg, D., and Hladnik, L. (1996). "Slenderness limit of class 3 I cross-sections made of high strength steel." *Journal of Constructional Steel Research*, 38(3), 201-217.  
 355  
 356 CEN (European Committee for Standardization). (2005). "Eurocode 3: Design of steel structures. Part 1-1: General rules and rules for buildings." EN 1993-1-1, Brussels, Belgium.  
 357  
 358 CEN (European Committee for Standardization). (2007). "Eurocode 3: Design of steel structures. Part 1-12: Additional rules for the extension of EN 1993 up to steel grades S 700." EN 1993-1-12, Brussels, Belgium.  
 359  
 360 Chan, T.-M., Zhao, X.L. and Young, B. (2015). Cross-section classification for cold-formed and built-up high strength carbon and stainless steel tubes under compression. *Journal of Constructional Steel Research*, 106, 289-295.  
 361  
 362 Chen, M.-T. and Young, B. (2019). Material properties and structural behavior of cold-formed steel elliptical hollow section stub columns. *Thin-Walled Structures*, 134, 111-126.  
 363  
 364 Fang, H. and Chan, T.-M. (2018). Axial compressive strength of welded S460 steel columns at elevated temperatures. *Thin-walled Structures*, 129, 213-224.  
 365  
 366 Gardner, L., Chan, T. M., and Abela, J. M. (2011). "Structural behaviour of elliptical hollow sections under combined compression and uniaxial bending." *Advanced Steel Construction*, 7(1), 86-112.  
 367  
 368 Gkantou, M., Theofanous, M., Wang, J., Baniotopoulos, C., Gardner, L. (2017). "Behaviour and design of high-strength steel cross-sections under combined loading." *Proceedings of the Institution of Civil Engineers – Structures and Buildings*, 170 (SB11), 841-854.  
 369  
 370 Hu, Y.F. and Chung, K.-F. (2017). Numerical study on residual stresses in high strength Q690 cold-formed circular hollow sections. *Proceedings of the 15th East Asia-Pacific Conference on Structural Engineering and Construction*, 11-13 October 2017, Xi'an, China.  
 371  
 372 Huang, Y., and Young, B. (2014). "Experimental investigation of cold-formed lean duplex stainless steel beam-columns." *Thin-Walled Struct.*, 76, 105-117.  
 373  
 374 Lee, C. H., Han, K. H., Uang, C. M., Kim, D. K., Park, C. H., and Kim, J. H. (2012). "Flexural strength and rotation capacity of I-shaped beams fabricated from 800 MPa steel." *Journal of Structural Engineering*, 139(6), 1043-1058.  
 375  
 376 Ma, J. L., Chan, T. M., and Young, B. (2015). "Material properties and residual stresses of cold-formed high strength steel hollow sections." *Journal of Constructional Steel Research*, 109, 152-165.  
 377  
 378 Ma, J. L., Chan, T. M., and Young, B. (2016a). "Experimental investigation on stub-column behavior of cold-formed high-strength steel tubular sections." *Journal of Structural Engineering*, 142(5), 04015174-1 to 04015174-11.  
 379  
 380 Ma, J. L., Chan, T. M., and Young, B. (2016b). "Experimental investigation of cold-formed high strength steel tubular beams." *Engineering Structures*, 126, 200-209.  
 381  
 382 Ma, J. L., Chan, T. M. and Young, B. (2017a). "Tests on high-strength steel hollow sections: a review." *Proceedings of the Institution of Civil Engineers – Structures and Buildings*, 170 (SB9), 621-630.  
 383  
 384 Ma, J. L., Chan, T. M. and Young, B. (2017b). Design of cold-formed high strength steel tubular beams. *Engineering Structures*, 151, 432-443.  
 385  
 386 Ma, J. L., Chan, T. M. and Young, B. (2018). "Design of cold-formed high strength steel tubular stub columns." *Journal of Structural Engineering*, 144(6), 04018063-1 to 04018063-10.  
 387  
 388 Nishino, F. and Tall, L. (1970). "Experimental investigation of the strength of T-1 steel columns." *Fritz Engineering Laboratory Report*, Lehigh University, Bethlehem, Pennsylvania.  
 389  
 390 Rasmussen, K. J. R. and Hancock, G. J. (1993). "Design of cold-formed stainless steel tubular members. I: columns." *J. Struct. Eng.*, 119(8), 2349-2367.  
 391  
 392 Rasmussen, K. J. R. and Hancock, G. J. (1995). "Test of high strength steel columns." *Journal of Constructional Steel Research*, 34, 27-52.  
 393  
 394 Rossi, B., Afshan, S. and Gardner, L. (2013). "Strength enhancements in cold-formed structural sections – Part II: Predictive models" *Journal of Constructional Steel Research*, 83, 189-196.  
 395  
 396 Sheehan, T., Dai, X. H., Chan, T. M. and Lam, D. (2012). "Structural response of concrete-filled elliptical steel hollow sections under eccentric compression." *Engineering Structures*, 45, 314-323.  
 397  
 398  
 399  
 400

401 Usami, T., and Fukumoto, Y. (1982). "Local and Overall Buckling of Welded Box Columns." *ASCE*, 108.

402 Wang, J., Afshan, S., Schillo, N., Theofanous, M., Feldmann, M. and Gardner, L. (2017). Material properties and

403 compressive local buckling response of high strength steel square and rectangular hollow sections. *Engineering*

404 *Structures*, 130, 297-315.

405 Wang, J. and Gardner, L. (2017). Flexural buckling of hot-finished high-strength steel SHS and RHS columns. *Journal of*

406 *Structural Engineering*, ASCE, 143(6), 04017028-1 to -12.

407 Yu, C. K., and Tall, L. (1968). "Welded built-Up and Rolled Heat-Treated "T-1" Steel Columns - A514 Steel Beam-

408 Columns." Lehigh University, Bethlehem, Pennsylvania.

409 Zhu, J. H., and Young, B. (2006). "Experimental Investigation of Aluminum Alloy Thin-Walled Tubular Members in

410 Combined Compression and Bending." *J. Struct. Eng.*, 132(12), 1955-1966.

411 Ziemian, R. D. (2010). *Guide to stability design criteria for metal structures, 6th edition*, John Wiley & Sons.

**Table 1.** SHS and RHS tensile coupon test results (Ma et al. (2015))

Section $B \times H \times t$ (mm)	Flat coupons			Corner coupons			Comparison
	$E$	$\sigma_{0.2f}$	$\sigma_u$	$E$	$\sigma_{0.2c}$	$\sigma_u$	$\frac{\sigma_{0.2c}}{\sigma_{0.2f}}$
	(GPa)	(MPa)	(MPa)	(GPa)	(MPa)	(MPa)	
H80×80×4	218	792	888	219	933	1005	1.18
H120×120×4	212	689	813	217	923	996	1.34
H140×140×6	201	663	808	210	859	959	1.30
H100×50×4	208	724	831	207	859	944	1.19
H200×120×5	207	738	846	205	895	970	1.21
V80×80×4	210	1005	1187	208	1187	1299	1.18
V120×120×4	204	960	1153	205	1114	1238	1.16

**Table 2.** Typical dimensions for specimens

Series	$L$	$B$	$H$	$t$	$R$	$r$
$B \times H \times t$ (mm)	(mm)	(mm)	(mm)	(mm)	(mm)	(mm)
H80×80×4	220	80.4	80.1	3.92	9.5	5.0
H120×120×4	310	120.9	120.9	3.92	8.0	4.0
H140×140×6	310	140.8	141.1	5.90	13.0	7.0
H50×100×4	220	50.6	100.2	3.94	8.5	3.5
H100×50×4	220	100.2	50.5	3.94	8.5	3.5
H120×200×5	490	120.6	200.3	4.93	13.0	7.5
H200×120×5	490	200.4	120.4	4.95	13.0	7.5
V80×80×4	220	80.4	80.2	3.95	10.0	6.0
V120×120×4	310	121.1	121.3	3.93	9.5	6.0

**Table 3.** Beam-column test results

Specimen	$e$ mm	$P_u$ kN	$M_{end,u}$ kN.m	$M_{mid,u}$ kN.m	Specimen	$e$ mm	$P_u$ kN	$M_{end,u}$ kN.m	$M_{mid,u}$ kN.m		
H80×80×4	e0	0.10	976	0.1	1.0	H200×120×5	e0	0.22	1745	0.4	2.5
	e10	10.07	755	7.6	9.4		e15	15.43	1388	21.4	22.4
	e20	18.67	618	11.5	13.1		e30	28.80	1149	33.1	34.3
	e40	40.33	435	17.5	18.9		e60	59.14	822	48.6	50.4
	e80	80.45	283	22.7	23.9		e60#	60.10	826	49.6	51.4
H120×120×4	e0	0.19	1211	0.2	1.0		e120	120.06	509	61.2	63.0
	e5	4.31	1200	5.2	6.2	H120×200×5	e0	1.08	1701	1.8	4.0
	e12	11.91	1036	12.3	13.3		e15	15.60	1603	25.0	27.4
	e30	29.62	788	23.3	24.4		e30	30.72	1451	44.6	47.0
	e60	57.91	576	33.4	34.4		e60	59.90	1243	74.5	77.3
	e120	118.63	366	43.4	44.6		e110	111.86	931	104.2	107.5
H140×140×6	e0	0.27	2434	0.7	0.9		e110#	110.58	931	103.0	106.5
	e15	13.27	2035	27.0	28.7	V80×80×4	e0	0.51	1252	0.6	2.2
	e35	35.55	1612	57.3	59.9		e10	8.05	995	8.0	11.3
	e70	68.64	1141	78.3	80.9		e20	21.76	794	17.3	20.2
	e100	100.87	824	83.1	86.2		e40	38.89	588	22.9	25.5
H50×100×4	e0	0.17	903	0.2	0.3		e80	80.45	346	27.8	29.7
	e8	7.91	768	6.1	7.2		V120×120×4	e0	0.02	1439	0.0
	e20	19.00	632	12.0	13.3	e12		12.97	1225	15.9	17.7
	e40	39.70	473	18.8	20.2	e30		29.16	926	27.0	28.7
	e100	99.09	257	25.5	26.8	e60		60.32	655	39.5	40.9
H100×50×4	e0	0.06	879	0.1	0.5	e60		59.99	672	40.3	41.2
	e5	3.71	738	2.7	3.6	e120		119.04	394	46.9	48.1
	e10	8.86	608	5.4	6.5	e140		140.95	359	50.6	51.7
	e25	23.06	412	9.5	10.6	Note:					
	e50	49.28	252	12.4	13.4		1. eX indiates a specimen with a nominal eccentricity of X mm.				
	e50#	49.54	255	12.6	13.5		2. # inidicates repeated tests.				

26  
27  
28  
29  
30  
31  
32  
33  
34

**Table 4.** Measured bending moment capacities (Ma et al. (2016b))

Specimen	Ultimate moment capacity
	$M_u$ (kNm)
H80×80×4-B	28.1
H120×120×4-B	56.1
H140×140×6-B	121.7
H100×50×4-B	16.9
H50×100×4-B	30.9
H200×120×5-B	90.3
H120×200×5-B	157.0
V80×80×4-B	37.5
V120×120×4-B	68.6

**Table 5.** Comparison with codes and FE results

Num. of tests: 51	$P_u/P_{AISC}$	$P_u/P_{AS4100}$	$P_u/P_{EC3}$	$P_u/P_{FE}$
mean	1.13	1.21	1.16	0.98
COV	0.081	0.075	0.067	0.042
$\phi$	0.9	0.9	1.0	
$\beta$	2.94	3.01	2.51	

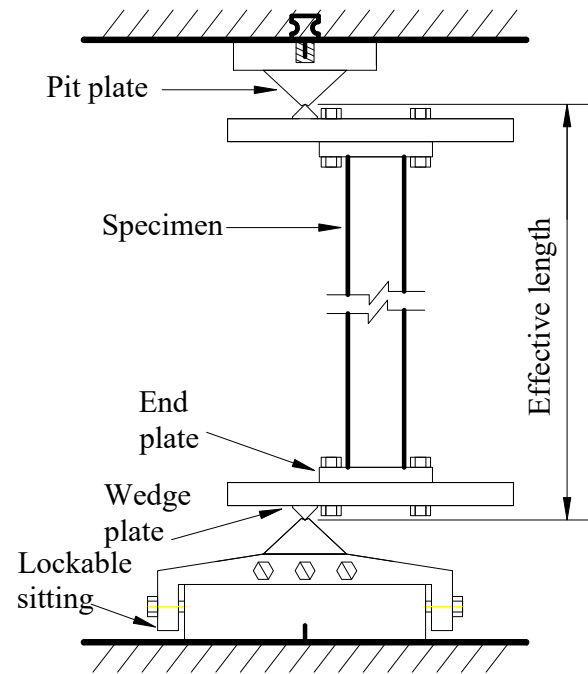
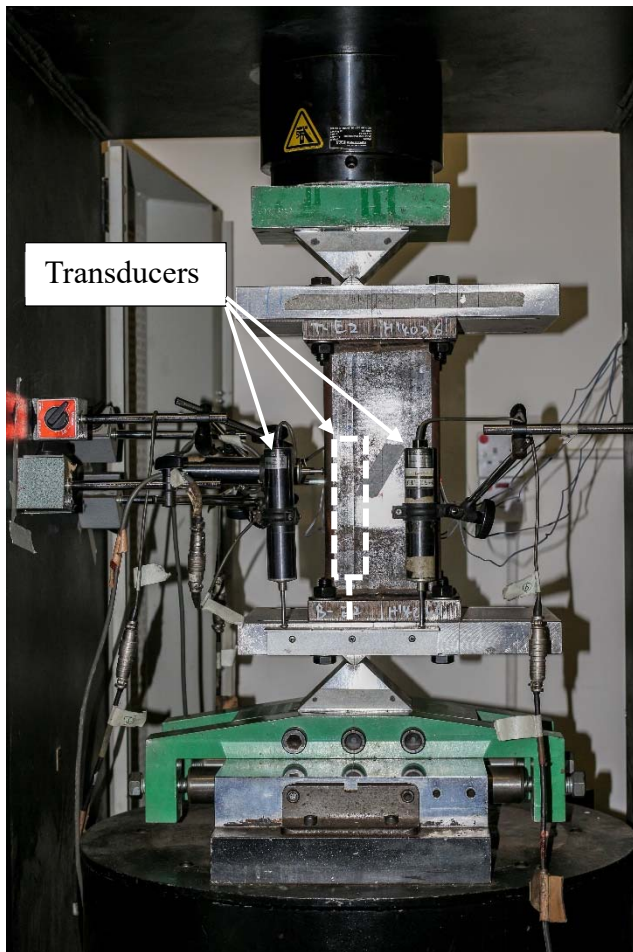


**Fig. 1 .** Experimental and schematic arrangement for beam-column tests

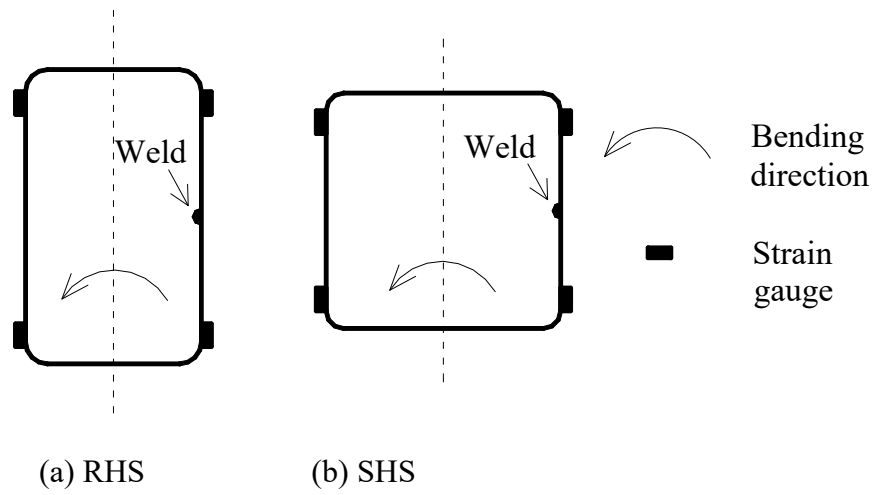


**Fig. 2 .** Arrangement of strain gauges for beam-columns

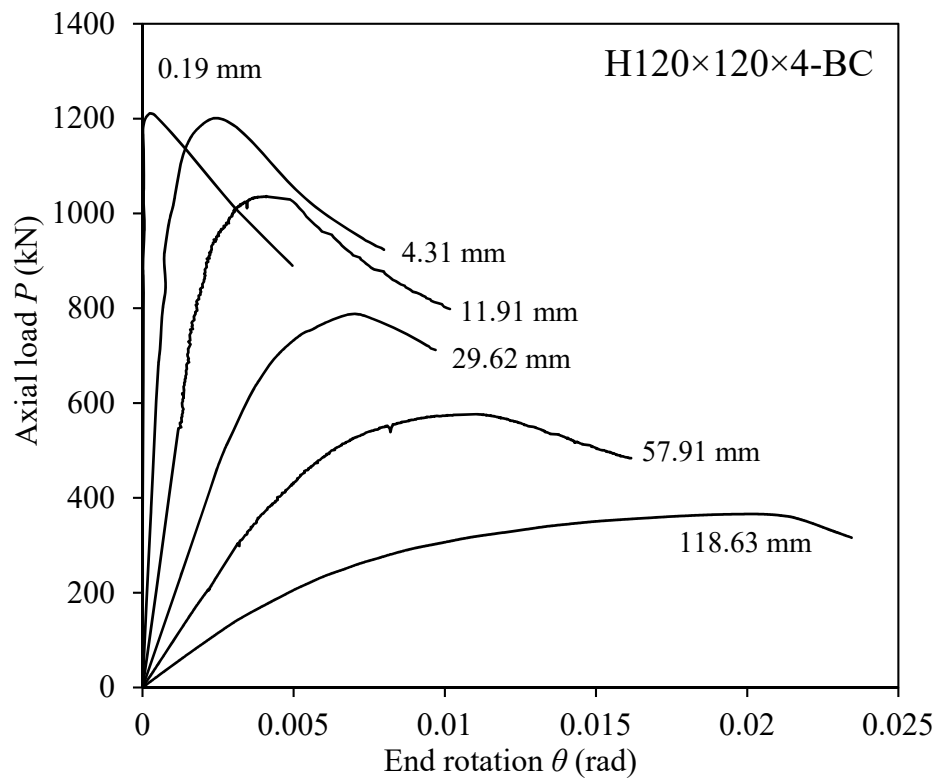


**Fig. 3 .** Axial load versus end rotation curves for H120×120×4-BC

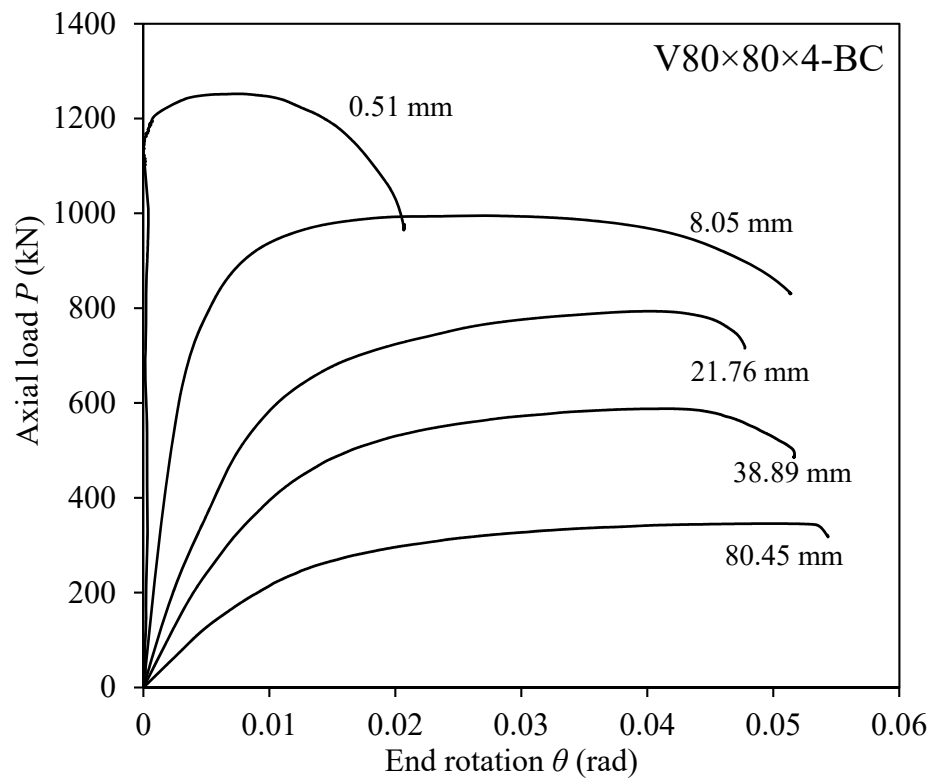
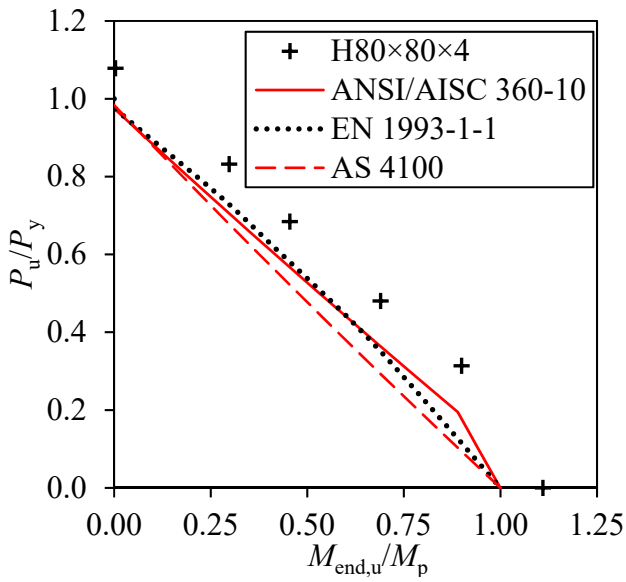
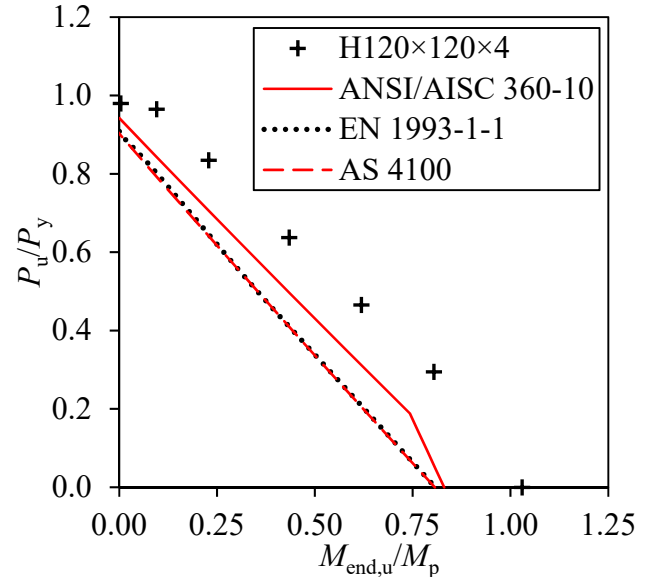


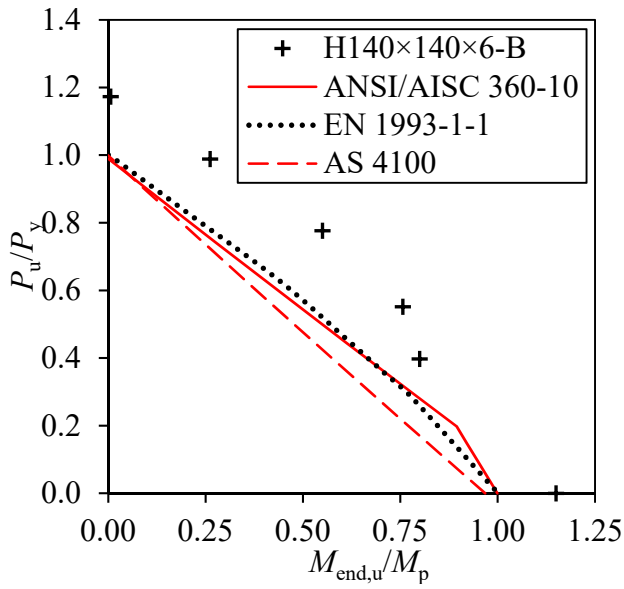
**Fig. 4 .** Axial load versus end rotation curves for V80×80×4-BC



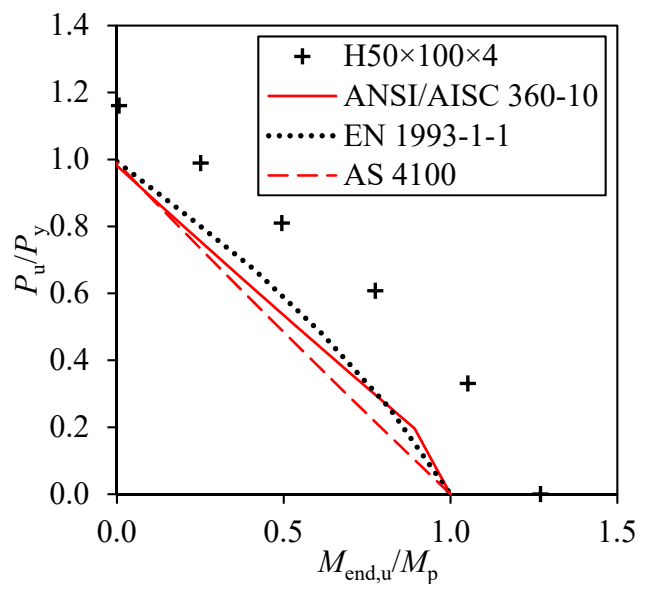
a) H80×80×4



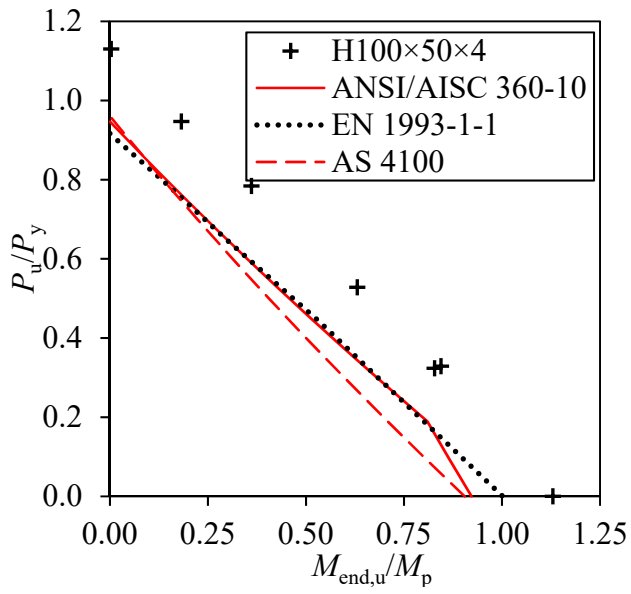
b) H120×120×4



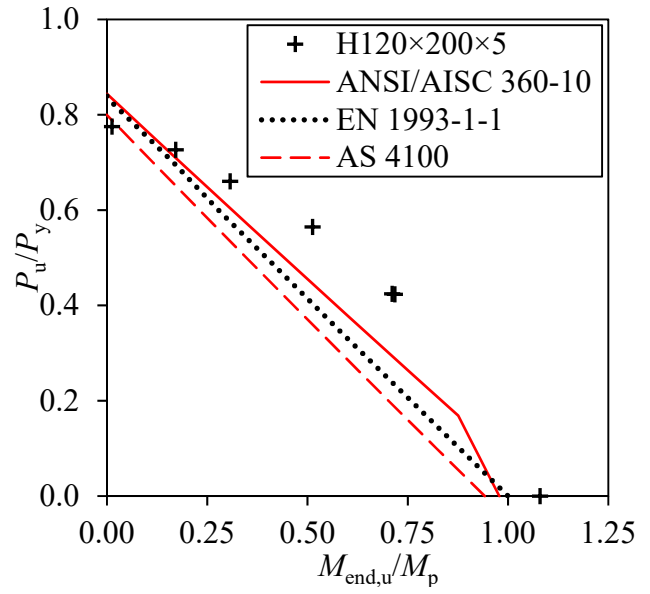
c) H140×140×6



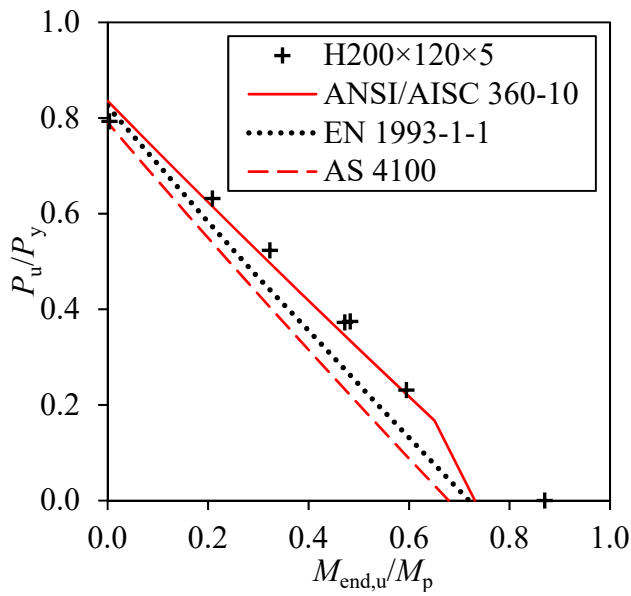
d) H50×100×4



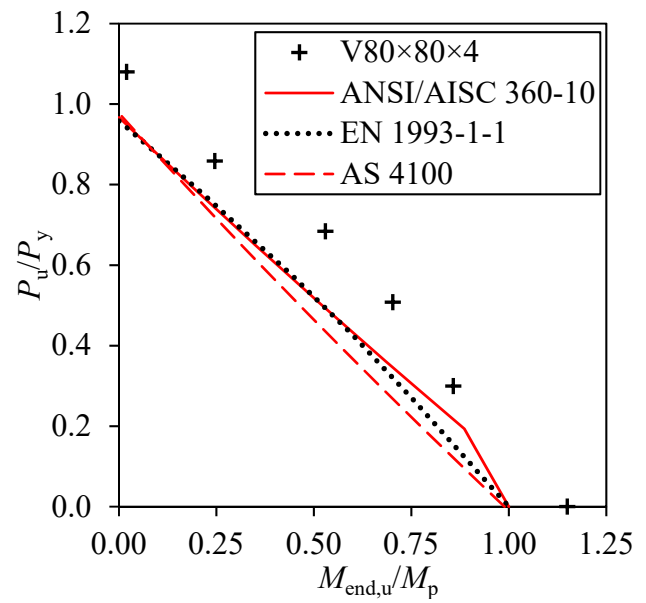
e) H100x50x4



f) H120x200x5



g) H200x120x4



h) V80x80x5

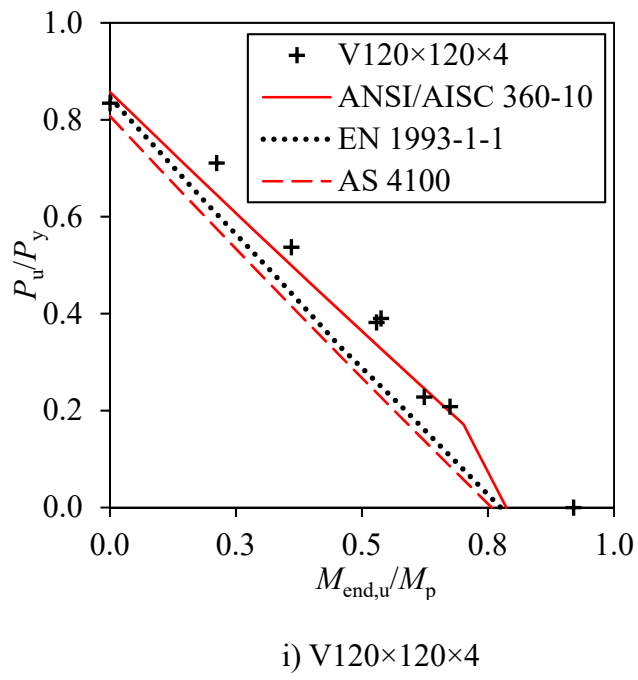


**Fig. 5 .** Comparison of interaction curves

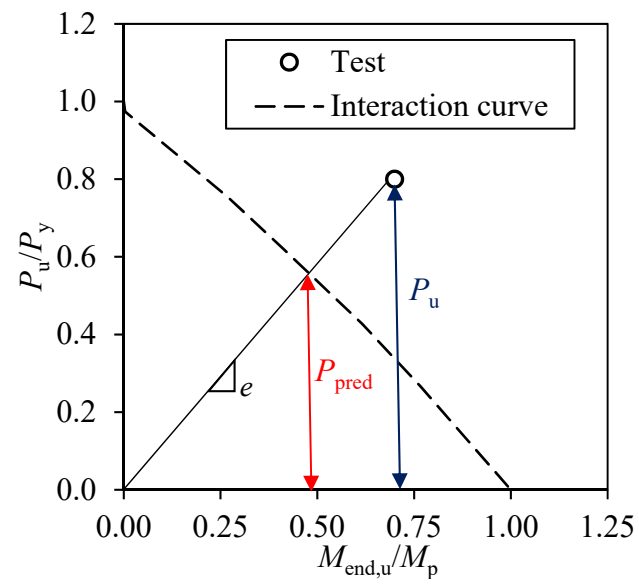


**Fig. 6 .** Illustration for comparison between tests and predictions from codes

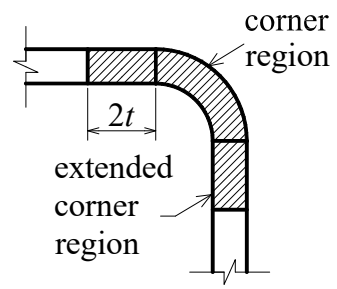


**Fig. 7 .** Extension of corner material property to flat portions

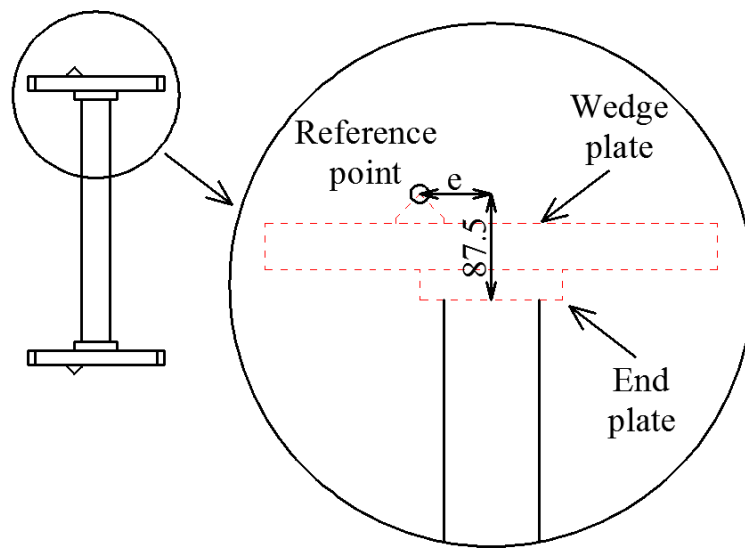


**Fig. 8 .** Location of reference point

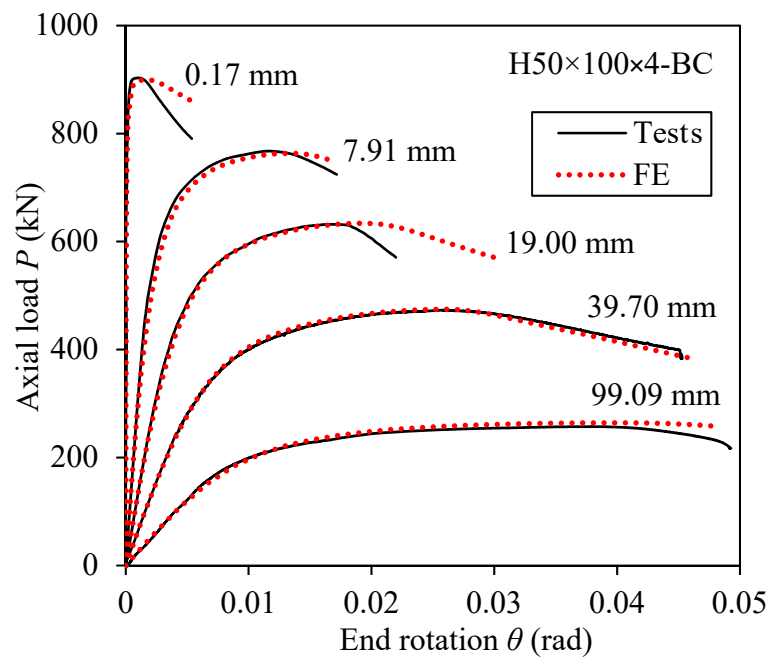


**Fig. 9 .** Experimental and numerical load-end rotation curves for H50×100×4-BC



**Fig. 10 .** Comparison of failure modes between test and numerical results for H120×120×4-BC-e30



**Fig. 11 .** Comparison of failure modes between test and numerical results for H120×200×5-BC-e60